Bistatic Frequency-Swept Microwave Imaging: Principle, Methodology and Experimental Results

Ding-Bing Lin, *Student Member, IEEE,* and Tah-Hsiung Chu, *Member, IEEE*

Abstract—**The basic principle, methodology and experimental results of frequency-swept microwave imaging of continuous shape conducting and discrete line objects in a bistatic scattering arrangement are presented. Theoretical analysis is developed under the assumptions of plane wave illumination and physical optics approximation. The measurement system and calibration procedures are implemented based on the plane wave spectrum analysis. Images of three different types of scattering objects reconstructed from the experimental data measured in the frequency range 7.5–12.5 GHz are shown in good agreement with the scattering object geometries. The results demonstrate that the developed bistatic frequency-swept microwave imaging system has potential as a cost-effective tool for the application of remote sensing, imaging radar, and nondestructive evaluation.**

I. Introduction

IT HAS BEEN of long standing interest in inverse scattering problems to develop analytical method and measurement system that enable one to use the information in the measured electromagnetic field to infer the geometrical shape, or the material characteristics of the unknown scattering object [1]. Microwave imaging is cataloged as an inverse scattering problem, and finds its application in imaging radar, remote sensing, nondestructive evaluation, and biological diagnosis etc., because microwaves can penetrate fog, cloud, and a variety of dielectric materials.

It is known that the Bojarski's identity forms the basis of microwave imaging of a perfectly conducting object in the far-field backward monostatic scattering arrangement [2], [3]. A microwave imaging system with high image resolution can be achieved by extending the effective area of the physical recording aperture using frequency, angular and polarization diversity techniques. With the use of Bojarski's identity and frequency-swept technique, high-resolution microwave image of conducting objects has been experimentally demonstrated in [4] and [5]. However, in the monostatic scattering arrangement the scattering object is rotated (i.e., angular diversity technique) in order to acquire the object scattering information at different viewing and illumination angles.

This paper studies the frequency-swept microwave imaging in a bistatic scattering arrangement in which, by using the plane wave expansion of the scattered field over a linear array, the far-field criterion does not meet as that in the Bojarski's identity. With the use of linear receiving array and frequency diversity technique, the images are shown to be reconstructed from the acquired object scattered field in a cost-effective sense without the use of planar array or time-consuming angular diversity technique.

The aim of this paper is to develop and experimentally demonstrate a cost-effective data acquisition and processing scheme for use in a bistatic frequency-swept microwave imaging system. This paper begins with the theoretical aspects of frequency-swept microwave imaging of perfectly conducting object in the bistatic backward scattering arrangement which was found to be a cost-effective approach compared with the multiview, single-frequency forward scattering arrangement [6]. Analtyical results to be developed in Section II show that the image can be reconstructed via Fourier inversion of the acquired Fourier space data under the assumptions of plane wave illumination and physical optics approximation. Note only a two-dimensional bistatic scattering measurement system is studied in this paper due to the simplicity and practical consideration of using linear array instead of the three-dimensional analysis described in [6].

According to the formulation of image reconstruction to be given in Section II, the scattering object is normally (zero incidence angle) illuminated by a plane wave, and its scattered field is recorded by a linear receiving array. In our measurement system, a rectangular horn antenna and an open-ended rectangular waveguide probe mounted on a linear scanner are used for transmitting and receiving wide-band signals. The error caused from the imperfect plane wave illumination is neglected, and the receiving probe response will be calibrated for the determination of the Fourier space data of scattering object. However, the mutual coupling effect in a linear array is not considered in this arrangement.

The methodology on which the calibration procedure to be developed in Section III is based on the representation of both the scattered field (or input signal to the receiving probe) and the measured signal from the probe as a superposition of plane waves each traveling in different direction with different amplitudes [7], [8]. A calibration equation is then derived to relate the measured Fourier space data to the calibrated Fourier space data. In Section IV the images reconstructed from the experimental data using the developed calibration procedures show that the developed frequency-swept bistatic microwave imaging system is capable of cost-effectively yielding images in good agreement with the scattering object geometries.

Manuscript received February 25, 1992; revised September 14, 1992. This work was supported by the National Science Council, Republic of China, under Grant NSC 81-0404-E002-580.

The authors are with the Electrical Engineering Department, National Taiwan University, Taipei 106-17, Taiwan, Republic of China.

IEEE Log Number 9207415.

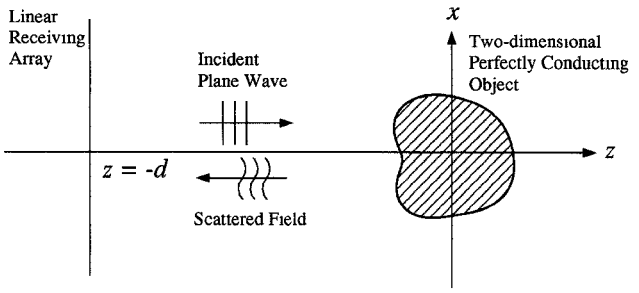

Fig. 1. Two-dimnensional bistatic scattering geometry.

II. Principle

In this section, we will relate the bistatic scattering properties to the microwave image reconstruction algorithm for two-dimensional continuous shape conducting and discrete line objects in the bistatic scattering arrangement as shown in Fig. 1. In the following derivation the scattering object is assumed to be infinitely long in the y-direction (normal to the x-z plane), and is illuminated by a normally incident TM-polarized plane wave

$$\boldsymbol{E}^i(\boldsymbol{r}) = \hat{y} E_0 e^{-jk_0 \hat{z}\cdot\boldsymbol{r}}, \tag{1}$$

$$\boldsymbol{H}^i(\boldsymbol{r}) = \frac{1}{\eta}\hat{z} \times \boldsymbol{E}^i(\boldsymbol{r}) \tag{2}$$

where $k_0 = \omega/c$ is the wave number, E_0 is the complex field amplitude, $\eta = \sqrt{\mu_0/\epsilon_0}$ is the intrinsic impedance in free space, and $\exp(j\omega t)$ time dependence is implied.

The scattered field over a linear array in the x-direction located at $z = -d$ (shown in Fig. 1) for the case of a perfectly conducting object satisfying the physical optics approximation is given as

$$\begin{aligned}\boldsymbol{E}_c^s(x, z=-d, k_0) &= -jk_0\eta \int_{C_{ill}} 2\hat{n}(\boldsymbol{r}') \\ &\quad \times \boldsymbol{H}^i(\boldsymbol{r}') G(|\boldsymbol{r}-\boldsymbol{r}'|)\, d\boldsymbol{r}'\end{aligned} \tag{3}$$

where C_{ill} is the illuminated object contour, $\hat{n}(\boldsymbol{r}')$ is the outward unit normal vector of C_{ill} at $\boldsymbol{r}'$, and

$$G(|\boldsymbol{r}-\boldsymbol{r}'|) = \frac{1}{4j} H_0^{(2)}(k_0|\boldsymbol{r}-\boldsymbol{r}'|) \tag{4}$$

is the Green's function in free space.

Similarly, for the case of discrete line scatterers with the current density induced on the ith line scatterer at $\boldsymbol{r}_i'$ expressed as

$$\boldsymbol{J}(\boldsymbol{r}) = \frac{j}{k_0\eta}\sigma(\boldsymbol{r}_i')\boldsymbol{E}^i(\boldsymbol{r}_i')\delta(\boldsymbol{r}-\boldsymbol{r}'), \tag{5}$$

i.e., the line scatterers scatter isotropically with no mutual coupling and having reflectivity $\sigma(\boldsymbol{r}_i')$, the scattered field over a linear array in the x-direction located at $z = -d$ is given as

$$\boldsymbol{E}_d^s(x, z=-d, k_0) = \sum_i \sigma(\boldsymbol{r}_i')\boldsymbol{E}^i(\boldsymbol{r}_i')G(|\boldsymbol{r}-\boldsymbol{r}_i'|). \tag{6}$$

On assuming the polarization state of receiving array in the y -direction, the scattered field recorded by the linear array at $z = -d$ becomes

$$U^s(x, z=-d, k_0) = \hat{y}\cdot\boldsymbol{E}^s(x, z=-d, k_0). \tag{7}$$

Therefore (3) can be expressed as

$$\begin{aligned}U_c^s(x, z=-d, k_0) &= \hat{y}\cdot\boldsymbol{E}_c^s(x, z=-d, k_0) \\ &= -jk_0E_0 \int\int O_c(\boldsymbol{r}')e^{-jk_0\hat{z}\cdot\boldsymbol{r}'}\cdot G(|\boldsymbol{r}-\boldsymbol{r}'|)\, d^2\boldsymbol{r}'\end{aligned} \tag{8}$$

where

$$O_c(\boldsymbol{r}') = -2\hat{n}(\boldsymbol{r}')\cdot\hat{z}\delta(C(\boldsymbol{r}')) \tag{9}$$

is defined as the scattering function of the perfectly conducting object which is related to the object shape, and $\delta(C(\boldsymbol{r}'))$ is a one-dimensional Dirac delta function with its argument defined as

$$C(\boldsymbol{r}')\begin{cases} =0 & \text{as } \boldsymbol{r}' \in C_{ill} \\ \neq 0 & \text{elsewhere}\end{cases} \tag{10}$$

which reduces the surface integral in (8) to the line integral in (3).

Similarly by defining the scattering function of the discrete line objects which is related to the distribution of each line scatterer as

$$O_d(\boldsymbol{r}) = \sum_i \sigma(\boldsymbol{r}_i')\delta(\boldsymbol{r}-\boldsymbol{r}_i') \tag{11}$$

where $\delta(\boldsymbol{r}-\boldsymbol{r}_i')$ is a two-dimensional Dirac delta function, the summation in (6) becomes the surface integral given as

$$\begin{aligned}U_d^s(x, z=-d, k_0) &= \hat{y}\cdot\boldsymbol{E}_d^s(x, z=-d, k_0) \\ &= E_0 \int\int O_d(\boldsymbol{r}')e^{-jk_0\hat{z}\cdot\boldsymbol{r}'} \cdot G(|\boldsymbol{r}-\boldsymbol{r}'|)\, d^2\boldsymbol{r}'\end{aligned} \tag{12}$$

Note that (12) is similar to (8) except for the scaling factor outside the integral and the definition of scattering function. Therefore, for the simplicity and unification of the following formulation, (12) and (8) can be rewritten as

$$U^s(x, z=-d, k_0) = \kappa \int\int O(\boldsymbol{r}')e^{-jk_0\hat{z}\cdot\boldsymbol{r}'}G(|\boldsymbol{r}-\boldsymbol{r}'|)\, d^2\boldsymbol{r}'. \tag{13}$$

For the continuous scattering object, κ and $O(\boldsymbol{r}')$ are $-jk_0E_0$ and the microwave image defined by the scattering function given in (9) respectively. For the discrete scattering object, κ and $O(\boldsymbol{r}')$ are E_0 and the microwave image defined by the scattering function given in (11)

By using the plane wave expansion of the Green's function [10]

$$G(|\boldsymbol{r}-\boldsymbol{r}'|) = \frac{1}{2\pi}\int \frac{-j}{2\gamma}e^{-j[\gamma|-d-z'|+k_x(x-x')]}\, dk_x \tag{14}$$

where $\boldsymbol{r} = x\hat{x} - d\hat{z}, \boldsymbol{r}' = x'\hat{x} + z'\hat{z}$, and

$$\gamma = \begin{cases}\sqrt{k_0^2 - k_x^2} & \text{as } |k_x| \le k_0 \\ -j\sqrt{k_x^2 - k_0^2} & \text{as } |k_x| > k_0,\end{cases} \tag{15}$$

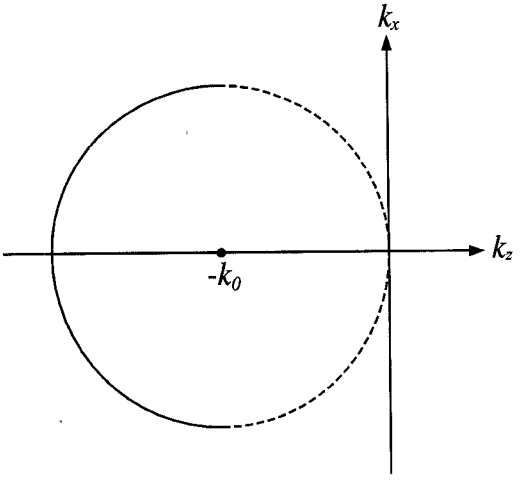

Fig. 2. Fourier slice acquired in the backward scattering arrangement with single-frequncy (wavenumber k_0) plane wave illumination.

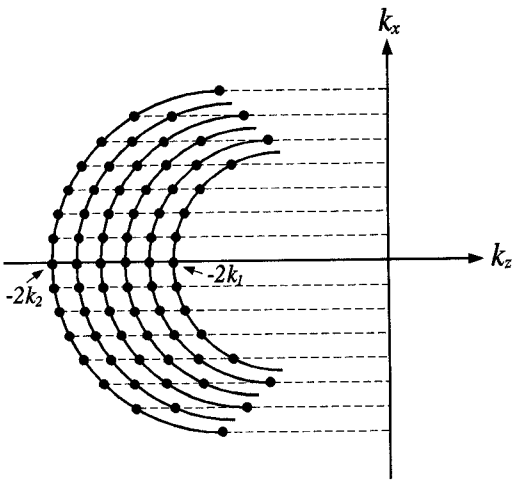

Fig. 3. Fourier space data acquired in the backward scattering arrangement using frequency diversity technique with k_0 stepped from k_1 to k_2.

and one-dimensional Fourier transforming the resulting expression of $U^s(x, z = -d, k_0)$ in the x-direction, one can obtain

$$\tilde{U}^s(k_x, z = -d, k_0) = \frac{-j\kappa}{2\gamma} e^{-\jmath\gamma d} \tilde{O}(k_x, -\gamma - k_0). \tag{16}$$

In deriving (16), the one-dimensional Fourier transformation of $U^s(x, z = -d, k_0)$ in the x-direction is defined as

$$\tilde{U}^s(k_x, z = -d, k_0) = \int U^s(x, z = -d, k_0) e^{jk_x x}\, dx, \tag{17}$$

whereas the two-dimensional Fourier transformation of the scattering function $O(\boldsymbol{r})$ is defined as

$$\tilde{O}(\boldsymbol{k}) = \int\int O(\boldsymbol{r}) e^{j\boldsymbol{k}\cdot\boldsymbol{r}}\, d^2\boldsymbol{r} \tag{18}$$

where $\boldsymbol{k} = k_x\hat{x} + k_z\hat{z}$ is the wave vector in Fourier space.

After applying (15), the arguments of $\tilde{O}(\boldsymbol{k})$ in (16) are related by

$$k_x^2 + (k_z + k_0)^2 = k_0^2. \tag{19}$$

Equations (16) and (19) show that as a two-dimensional scattering object is illuminated by a normally incident plane wave, one-dimensional Fourier transforming the scattered field recorded in the bistatic backward scattering arrangement yields a semicircular slice centered at $(0, -k_0)$ with radius k_0 in the two-dimensional Fourier space $\tilde{O}(\boldsymbol{k})$ of the scattering function as the semicircle denoted by the solid line shown in Fig. 2. The dashed line given in Fig. 2 corresponds to the bistatic forward scattering arrangement, however, it was shown that this arrangement is not practical using the frequency-swept technique due to its limited Fourier space [6].

In order to reconstruct the scattering object image with high resolution, a large portion of Fourier space data can be acquired by linearly stepping the frequency of incident plane wave form f_1 to f_2. Both the radius and the center of semicircular slice shown by (19) will vary from k_1 and $(0, -k_1)$ to k_2 and $(0, -k_2)$ accordingly. The semicircle denoted by the solid line in Fig. 2 then extends to a fan-shaped section in the Fourier space as shown in Fig. 3. This is known as the frequency diversity technique. Therefore, the two-dimensional Fourier inversion of band-pass version of the limited Fourier space data yields the similar image of either the shape of illuminated portion of continuous scattering object or the distribution of discrete scattering objects. The above theoretical results can be extended to the three-dimensional case with incident plane wave illuminating in an arbitrary direction. In the following section, experimental measurement system and calibration procedure to acquire the Fourier space data will be described.

III. Measurement System and Calibration Procedure

Shown in Fig. 4 is the developed experimental system to measure the wide-band bistatic scattering data of test object in a backward scattering arrangement. In the measurement system, an Arra X820 rectangular horn antenna is used for transmitting wide-band signals, and an open-ended WR-90 rectangular waveguide mounted on a linear scanner is used as the receiving probe. The linear scanner consists of a stepping motor for moving the receiving probe along the dashed line shown in Fig. 4 to synthesize a linear receiving array. The stepping motor driver is controlled by HP3852A data control unit. The measurement system also includes Hughes 8010H traveling wave tube amplifier (TWTA), Avantek AWT-18235 low noise amplifier (LNA), and HP8510B network analyzer. The measurement system is automated with MicroVax 3500 via an IEEE-488 interface bus to perform instrument control, data acquisition, and signal processing.

The calibration procedures to be described in the following for the developed measurement system is based on the plane wave expansion, in which a monochromatic scalar wave can be represented as [8]

$$U(\boldsymbol{r}, k_0) = \frac{1}{2\pi} \int \tilde{A}(k_x, k_0) e^{-j\boldsymbol{k}\cdot\boldsymbol{r}}\, dk_x, \tag{20}$$

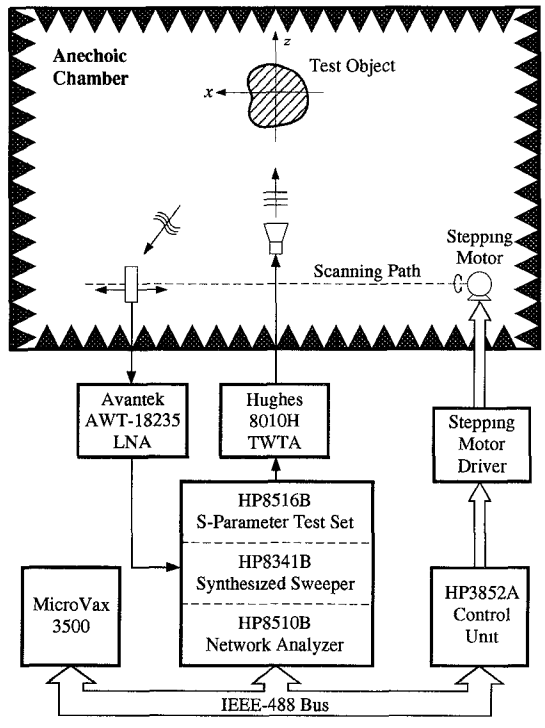

Fig. 4. Automated wide-band bistatic scattering measurement system.

i.e., a superposition of plane waves each traveling in different direction of $\boldsymbol{k} = k_x\hat{x} + k_z\hat{z}$ with amplitude $\tilde{A}(k_x, k_0)$ defined as the plane wave spectrum (PWS) of $U(\boldsymbol{r}, k_0)$. In (20) the wave vector $\boldsymbol{k}$ satisfies the dispersive relationship

$$k_x^2 + k_z^2 = k_0^2. \tag{21}$$

In the measurement system, the receiving probe is oriented in the z-direction as the transmitting horn antenna which gives a normally incident TM-polarized plane wave. By ignoring the effects due to the imperfect plane wave illumination from horn antenna and the multiple reflection between the antennas and test object, according to (16), (17), and (20) the scattered field at the receiving probe position can be expressed as

$$U_i^s(x, z = -d, k_0) = \frac{1}{2\pi}\int \tilde{A}_i(k_x, k_0)e^{-j[k_x x + (-\gamma)(-d)]}\,dk_x \tag{22}$$

where

$$\tilde{A}_i(k_x, k_0) = \tilde{I}_i(k_x, k_0) + \frac{-j\kappa}{2\gamma}\tilde{O}(k_x, -\gamma - k_0) \tag{23}$$

is called the PWS of the wave represented by (22), and $\tilde{I}_i(k_x, k_0)$ is the PWS of an additive isolation error to account for the residual reflection of the empty room.

Note the wave represented by (22) is not a quantity directly measurable. By considering the error associated with both the receiving probe response and the measurement system frequency response as a filter designated as $\tilde{R}(k_x, k_0)$ in the plane wave spectrum domain, the measured wide-band scattered field over the linear array can then be expressed as

$$U_m^s(x, z = -d, k_0) = \frac{1}{2\pi}\int \tilde{A}_0(k_x, k_0)e^{-j[k_x x + (-\gamma)(-d)]}\,dk_x \tag{24}$$

where

$$\begin{aligned}\tilde{A}_0(k_x, k_0) &= \tilde{I}_0(k_x, k_0) + \tilde{A}_i(k_x, k_0)\tilde{R}(k_x, k_0)\\ &= \tilde{I}(k_x, k_0) + \frac{-j\kappa}{2\gamma}\tilde{O}(k_x, -\gamma - k_0)\tilde{R}(k_x, k_0)\end{aligned} \tag{25}$$

is the PWS of the wave represented by (24), $\tilde{I}_0(k_x, k_0)$ is the PWS of the isolation error resulting from the coupling between transmitting and receiving antennas, and

$$\tilde{I}(k_x, k_0) = \tilde{I}_0(k_x, k_0) + \tilde{I}_i(k_x, k_0)\tilde{R}(k_x, k_0). \tag{26}$$

By one-dimensional Fourier transforming the measured scattered field represented by (24) in x-direction, one can obtain

$$\begin{aligned}\tilde{U}_m^s(k_x, z = -d, k_0) = \tilde{I}(k_x, k_0)e^{-j\gamma d} + \frac{-j\kappa}{2\gamma}e^{-j\gamma d}\\ \cdot \tilde{O}(k_x, -\gamma - k_0)\tilde{R}(k_x, k_0)\end{aligned} \tag{27}$$

which establishes a relationship between the calibrated Fourier space data and the measured Fourier space data. In (27) the first part is an isolation error term, and it can be directly acquired by one-dimensional Fourier transforming the signal measured without locating any scattering object inside the anechoic chamber. The second part is the product of three terms, the first term is referred as the range-phase term, the second term is the desired calibrated values of the two-dimensional Fourier transformation of the scattering function distributed on a semicircular slice in the Fourier space, and the third term is associated with the receiving probe and system frequency responses.

For a reference scattering object (27) becomes

$$\begin{aligned}\tilde{U}_{ref}^s(k_x, z = -d, k_0) = \tilde{I}(k_x, k_0)e^{-j\gamma d} + \frac{-j\kappa}{2\gamma}e^{-j\gamma d}\\ \cdot \tilde{O}_{ref}(k_x, -\gamma - k_0)\tilde{R}(k_x, k_0)\end{aligned} \tag{28}$$

where $\tilde{U}_{ref}^s(k_x, z = -d, k_0)$ and $\tilde{O}_{ref}(k_x, -\gamma - k_0)$ are the measured and calculated Fourier space data of the reference object used to eliminate the error terms given in (27). Therefore, from (27) and (28) the calibrated Fourier space data can be acquired as

$$\begin{aligned}\tilde{O}(k_x, -\gamma - k_0) = \frac{\tilde{U}_m^s(k_x, z = -d, k_0) - \tilde{I}(k_x, k_0)e^{-j\gamma d}}{\tilde{U}_{ref}^s(k_x, z = -d, k_0) - \tilde{I}(k_x, k_0)e^{-j\gamma d}}\\ \cdot \tilde{O}_{ref}(k_x, -\gamma - k_0).\end{aligned} \tag{29}$$

Summarized as follows are the calibration procedures based on the calibration equation (29):

1. Measure the wide-band isolation error using linear scanner in the empty room.
2. Positioning the reference object then the test object, measure the wide-band bistatic scattered fields then perform one-dimensional Fourier transformation after subtracting the wide-band isolation error measured in step (1).
3. Calibrate the Fourier space data of the test object using (29).

4. Use linear interpolation to acquire the Fourier space data in rectangular format for two-dimensional inverse fast Fourier transformation.

Note in step (3) one-dimensional Fourier transformation of the isolation error is not required, and it can be directly subtracted from the measured scattered field data in step (2).

IV. Experimental Results

Based on the above measurement system and calibration procedures, given in this section are the experimental results of three different types of scattering object: (a) a metallic cylinder with length 91 cm and radius $a = 15$ cm used as a continuous scattering object, (b) four distributed metallic thin cylinders with length 113 cm and radius $a = 0.5$ cm used as discrete line scatterers, and (c) a 1 : 100 scale metal covered B-52 model aircraft used as a complex scattering object, for demonstrating the performance of the developed frequency-swept bistatic microwave imaging system.

Before presenting the experimental results the sampling criteria and resolution of the developed imaging system are discussed in the following.

To avoid the aliasing effect, the stepping interval of linear scanner should satisfy

$$\delta x \leq \frac{\lambda_{\min}}{2} \tag{30}$$

where $\lambda_{\min}$ is the minimum wavelength (the maximum frequency). Similarly the frequency stepping interval requires

$$\delta f \leq \frac{c}{2\Delta r_{\max}} \tag{31}$$

where $\Delta r_{\max}$ is the maximum size of scattering object. The image resolution is inversely proportional to the effective area of Fourier space data. From Fig. 2, the fan-shaped section in the Fourier space, the range resolution becomes inversely proportional to the available bandwidth.

In the measurement, a 153.6-cm-long linear scanning positioner located at about $z = -95$ cm with reference to the center of test object positioner. The linear receiving array is synthesized by moving an open-ended WR-90 rectangular waveguide at 128 equally spaced positions. The frequency is stepped from 7.5 to 12.5 GHz for 51 frequency points. The reference object used for calibration is a metallic cylinder with length 113 cm and radius $a = 0.5$ cm.

In the type (a) test object, the range of ka is 23.6–39.3 radians, hence the measurement is in physical optics regime. Shown in Fig. 5(a) is the Fourier space data acquired from the frequency-swept bistatic microwave imaging system, and is in good agreement with the simulation result shown in Fig. 5(b). The reconstructed images from experimental data and simulation data are shown in Fig. 6(a) and (b). It is shown that the reconstructed image gives a partial circular ring image corresponding to the induced surface current distribution on the object illuminated region due to specular diffraction observed by the linear array. Therefore by extending the effective size of the linear array will not improve the image quality.

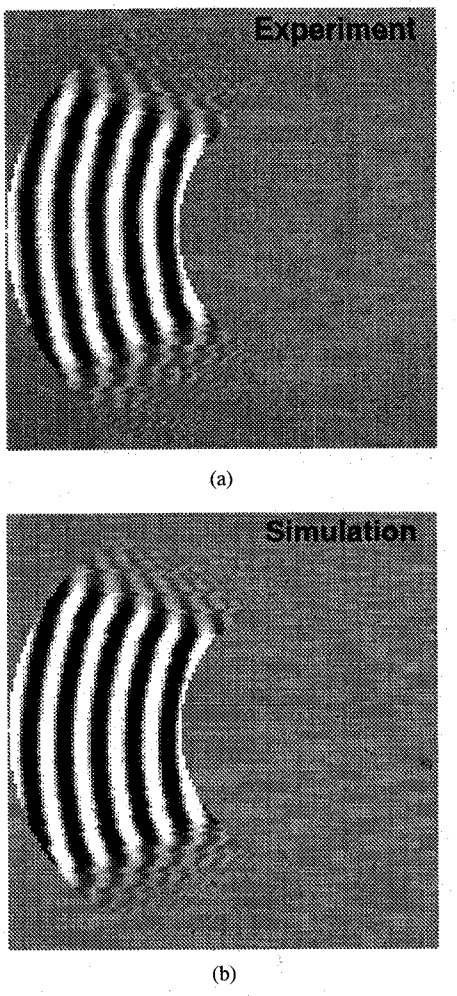

Fig. 5. (a) Measured and (b) simulated Fourier space data of a metallic cylinder with radius $a = 15$ cm.

The experimental results shown in Fig. 5 and 6 are in good agreement with the simulation results, in which an infinite long cylinder is illuminated by a plane wave, and the receiving antenna is treated as an ideal probe. This indicates that the data acquisition and calibration procedures described in the Section III remove the effects including the isolation error, the range-phase term, the nonideal receiving probe response, and the system frequency response.

In the type (b) test object, the range of ka is 0.79–1.31 radians, hence the thin cylinders can be treated as four line scatterers. Results of the Fourier space data and reconstructed image are shown in Fig. 7(a) and (b). The reconstructed image is in good agreement with the distribution of four thin cylinders given in Fig. 7(c).

For the complex object of a B-52 scale aircraft, it consists of discrete and continuous scattering centers contributed to the measured bistatic frequency-swept responses. Results of the Fourier space data and reconstructed image are shown in Fig. 8(a) and (b). The reconstructed image clearly indicates those scattering centers on the illuminated surface of test aircraft observed by the linear array. The image shown is not symmetrical with respect to the fuselage, because the assumption of infinite length in the y-direction is inadequate.

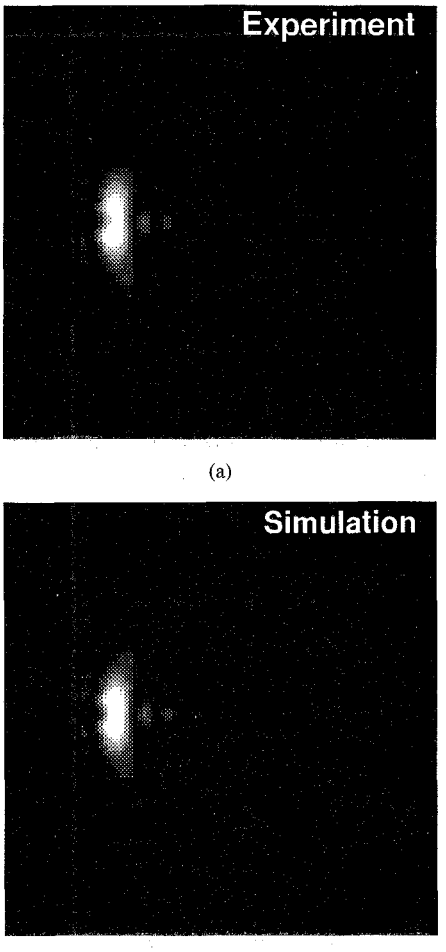

Fig. 6. Reconstructed images of metallic cylinder with radius $a = 15$ cm obtained from (a) measured and (b) simulated Fourier space data given in Fig. 5.

V. Conclusion

In this study, the frequency-swept microwave imaging of perfectly conducting objects in the bistatic scattering arrangement has been experimentally demonstrated to be able to retrieve the shape of continuous scattering object and the distribution of discrete scattering objects. By using the plane wave spectrum expansion of the scattered field measured from the receiving probe, the far-field criterion is then unncessary. Experimental results of three different types of scattering object illustrate the principle and methodology of the developed bistatic frequency-swept microwave imaging system.

In the analysis, the bistatic frequency-swept microwave imaging principle is developed under the physical optics approximation and two-dimensional scattering arrangement. It is known that the physical optics is inadequate as the dominant scattering mechanism involves the edge diffraction, multiple reflection, creeping waves, or traveling waves for a conducting object of complex shape [11]. Furthermore, study on the polarization effect in bistatic microwave imaging system is also important. However the reconstructed image of a three-dimensional B-52 scale model aircraft using the developed frequency-swept bistatic microwave imaging system yields the feature of the scattering complex object and delineates the correct geometrical relation and relative size. The results show that the described bistatic frequency-swept microwave imaging system can be a cost-effective approach in the use of imaging

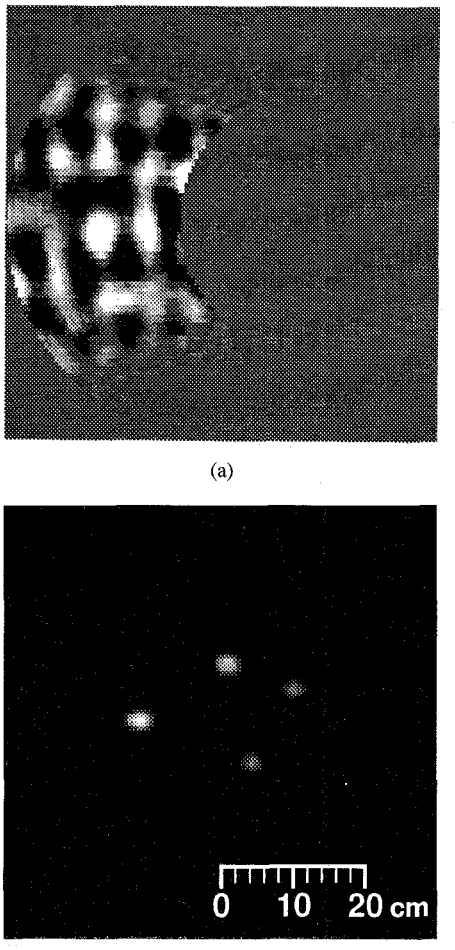

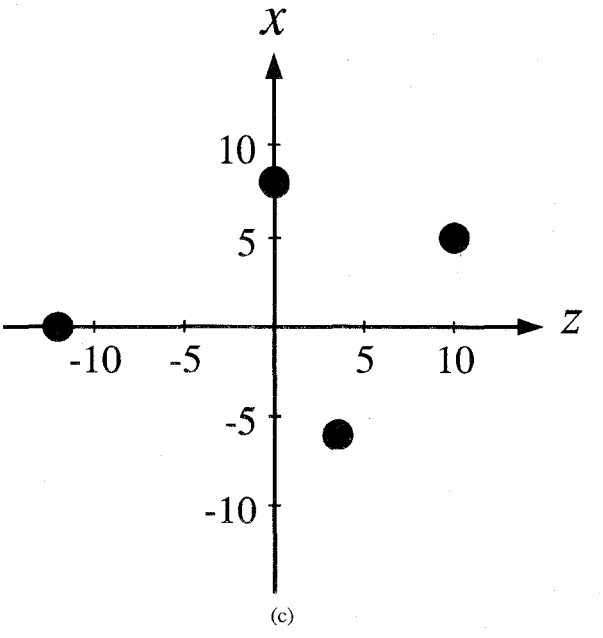

Fig. 7. (a) Fourier space data and (b) reconstructed image of four thin cylinders with (c) geometries at $(-12, 0)$ cm, (0, 8) cm, (3.5, -6) cm, and (10, 5) cm respectively.

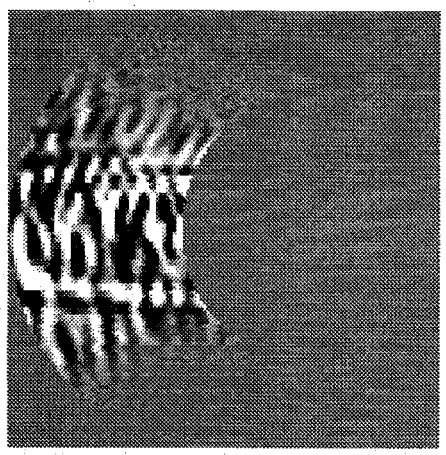

(a)

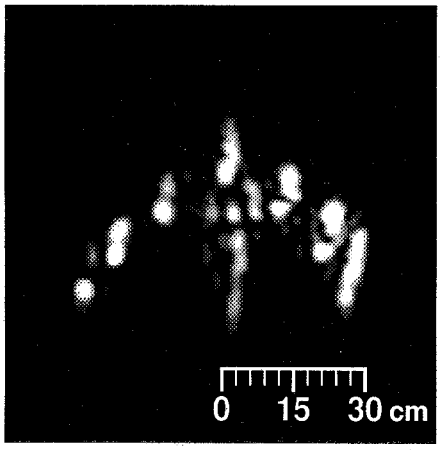

(b)

Fig. 8. (a) Fourier space data and (b) reconstructed image of a 1 : 100 scale B-52 model aircraft.

radar, remote sensing and nondestructive evaluation.

ACKNOWLEDGMENT

The authors wish to thank Dr. T.-J. Chen for his helpful discussion, and Mr. C.-Y. Chi for implementing the linear scanner.

REFERENCES

[1] H. P. Baltes, Ed., *Inverse Scattering Problems in Optics,* New York: Springer-Verlag, 1980.

[2] R. M. Lewis, "Physical optics inverse diffraction," *IEEE Trans. Antenna Propagat.,* vol. AP-24, pp. 308–314, May 1969.

[3] N. N. Bojarski, "A survey of physical optics inverse scattering identity," *IEEE Trans. Antennas Propagat.,* vol. AP-30, pp. 980–989, Sept. 1982.

[4] N. H. Farhat, C. L. Werner, and T. H. Chu, "Prospects for 3-D projective and tomographic imaging radar network," *Radio Sci.,* vol. 19, no. 15, pp. 1347–1355, Sept./Oct. 1984.

[5] N. H. Farhat, "Microwave diversity imaging and automated target identification based on models of neural networks," *Proc. IEEE,* vol. 77, pp. 670–680, May 1989.

[6] T. H. Chu and D. B. Lin, "Microwave diversity imaging of perfectly conducting objects in the near-field region," *IEEE Trans. Microwave Theory Tech.,* vol. 39, pp. 480–487, Mar. 1991.

[7] J. A. Stratton, *Electromagnetic Theory.* New York: McGraw-Hill, 1941, pp. 392–395.

[8] J. Appel-Hansen, "Antenna measurements," in *The Handbook of Antenna Design,* vol. 1. London: Peregrinus, ch. 8, 1982.

[9] R. F. Harrington, *Time-Harmonic Electromagnetic Fields.* New York: McGraw-Hill, pp. 125–128, 1961.

[10] E. Wolf, "Three-dimensional structure determination of semi-transparent objects from holographic data," *Optics Commun.,* vol. 1, no. 4, pp. 153–156, Sept./Oct. 1969.

[11] G. T. Ruck, D. E. Barrick, W. D. Stauart, and C. K. Krichbaum, *Radar Cross Section Handbook,* New York: Plenum Press, 1970.

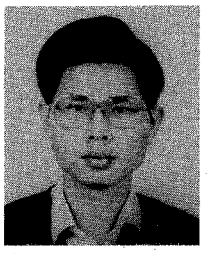

Ding-Bing Lin (S'89) was born in Taiwan on May 1, 1962. He graduated from the National Kaohsiung Institute of Technology, Kaohsiung, Taiwan in 1982, and received the M.S. degree in 1989 from the National Taiwan University, Taipei, Taiwan, where he is now working toward the Ph.D. degree, all in Electrical Engineering.

His research interests include microwave imaging systems and antenna measurement techniques.

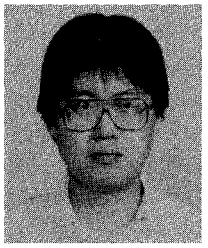

Tah-Hsiung Chu (M'87) was born in Taiwan on July 30, 1953. He received the B.S. degree from the National Taiwan University, Taipei, Taiwan in 1976, and the M.S. and Ph.D. degrees from the University of Pennsylvania in 1980 and 1983 respectively, all in electrical engineering.

From 1983 to 1986 he was a member of the technical staff, the Microwave Technology Center, at RCA David Sarnoff Research Center, Princeton, NJ. Since 1986 he has been on the faculty of the Department of Electrical Engineering at the National Taiwan University, where he is now Professor of Electrical Engineering. His research interests include microwave imaging systems and techniques, microwave circuit and subsystem design, electromagnetic theory, microwave measurement and calibration techniques, and digital and optical signal processing.